ADVANCED FUNCTIONAL MATERIALS
www.afm-journal.de

Balancing Packing Strength of End/Central Units Enables Binary Organic Solar Cells to Achieve 20.2% Efficiency

Peiran Wang, Xiangjian Cao, Wenkai Zhao, Yu Zhang, Zheng Xu, Zhe Zhang, Guanghui Li, Guankui Long, Xiangjian Wan, Chenxi Li, Zhaoyang Yao, Bin Kan,* and Yongsheng Chen**

The photodynamic processes in organic solar cells (OSCs) are largely determined by the intermolecular packing of photovoltaic materials, which makes the delicate tuning of packing characteristics through molecular structural tailoring crucially important. Herein, an asymmetric acceptor of CHFN is constructed to balance the effective packing areas or packing strength of end/central units in molecular skeletons. Compared to CH6F and CH17 with the symmetric structures, asymmetric CHFN possesses the more suitable crystallinity, superior fibrillar network morphology, and facilitated charge generation/transport in blended films, thus affording a remarkable PCE of 20.23% for CHFN-based binary OSCs, which is one of the highest efficiencies of binary OSCs based on asymmetric acceptors. This work highlights the great significance of end/central unit packing balance in achieving highly efficient OSCs.

1. Introduction

Organic solar cells (OSCs) with successively increased power conversion efficiencies (PCEs) have attracted widespread attention.[1–5] Currently, the PCE of OSCs has grown to over 20% largely due to the innovation of small molecule acceptors (SMAs).[6–10] Among them, the super star SMA of Y6 could contribute to a superior 3D molecular packing network that differs from other types of SMAs, which has been regarded as one of the determining factors for the excellent photovoltaic performance of Y-series SMAs.[11–14] Bearing these in mind, the optimization of molecular packing behaviors through delicate molecular structural modification should be crucially important if a better photovoltaic outcome is further expected.[15,16]

Recently, a series of SMAs with the two-dimensionally extended central unit were developed and displayed great potential for achieving the state-of-the-art OSCs.[17–20] Besides the influences on energy level distributions and light absorptions, the 2D conjugated central units could largely reconstruct the intermolecular packing modes of SMAs, thus providing an effective pathway to optimize the aggregated behaviors of SMAs and the nanoscale morphologies in blended films.[21,22] In addition, our recent work also disclosed that the excessive conjugated extension of central units will result in the disappearance of the end unit involved packing mode (like end-to-end), thereby destroying the desirable 3D packing network of SMAs.[23] These findings highlight the great significance of balanced end/central units packing in facilitating charge transfer/transport in blended films, and achieving highly efficient OSCs.

Herein, on the basis of the high-performance 2D extended SMA platform of CH6F[24] and CH17,[17] CHFN was constructed by changing one of the end units to afford an asymmetrical molecular backbone. Due to the different effective packing areas of end units in CH6F, CHFN, and CH17, the molecular packing modes determined by both central and end units may be tuned delicately. Moreover, the asymmetrical geometry of CHFN is also expected to lead to a quite different molecular packing behavior.[25–27] A systematic investigation revealed that CHFN possesses the more suitable crystallinity, superior fibrillar network morphology, and charge generation/transport in blended films. As a consequence, CHFN-based binary OSC affords an excellent binary OSC efficiency of 20.23%, much better than that of 19.20% for CH6F- and 19.00% for CH17-based devices. Note that CHFN has contributed the highest efficiency of binary OSCs based on asymmetric acceptors.

P. Wang, W. Zhao, G. Long, B. Kan
School of Materials Science and Engineering
National Institute for Advanced Materials
Nankai University
Tianjin 300350, China
E-mail: kanbin04@nankai.edu.cn

X. Cao, Y. Zhang, Z. Xu, Z. Zhang, G. Li, X. Wan, C. Li, Z. Yao, Y. Chen
State Key Laboratory and Institute of Elemento-Organic Chemistry
The Centre of Nanoscale Science and Technology and Key Laboratory of Functional Polymer Materials
Renewable Energy Conversion and Storage Center (RECAST)
College of Chemistry
Nankai University
Tianjin 300071, China
E-mail: zyao@nankai.edu.cn; yschen99@nankai.edu.cn

The ORCID identification number(s) for the author(s) of this article can be found under https://doi.org/10.1002/adfm.202518113

DOI: 10.1002/adfm.202518113

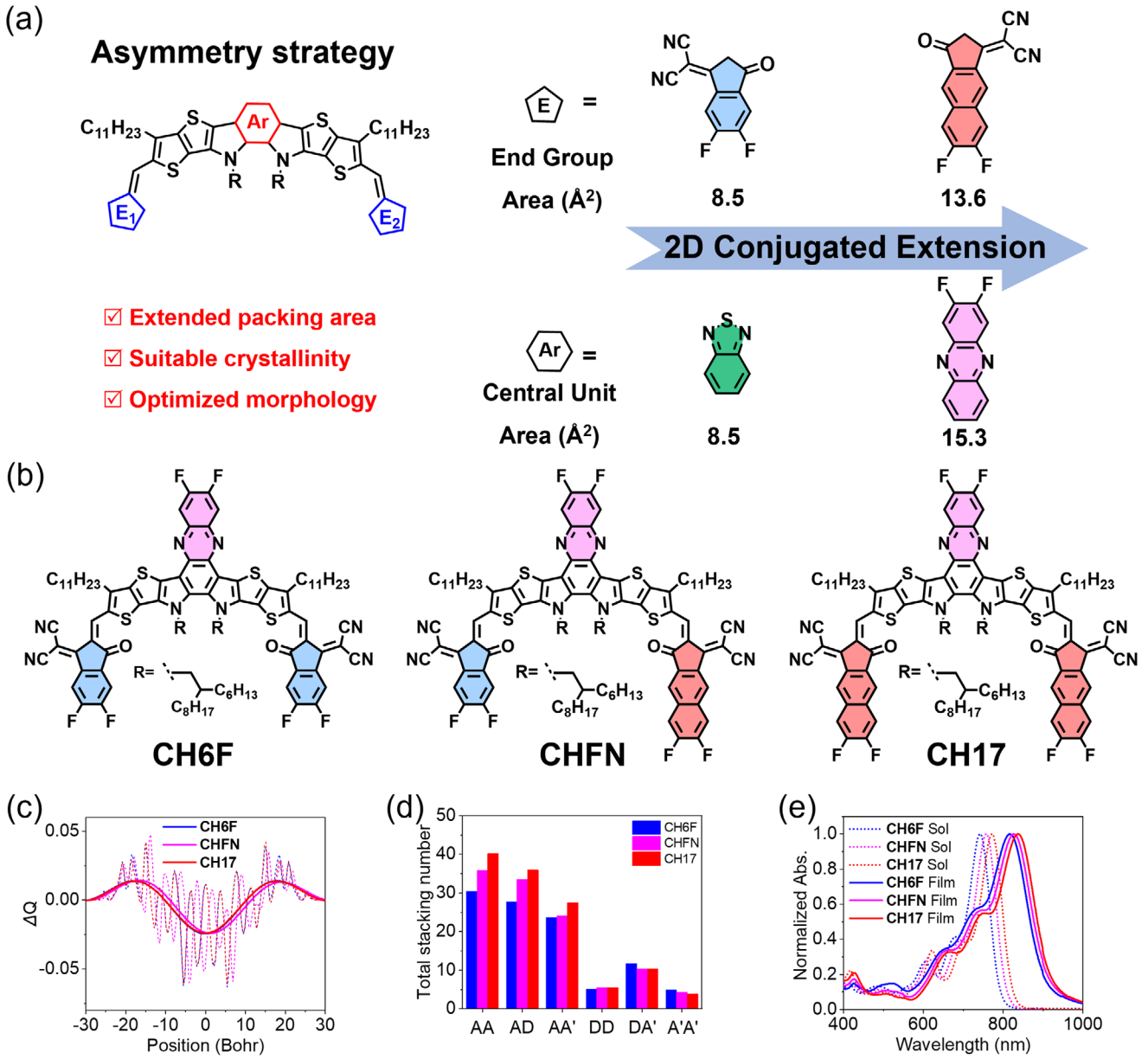

Figure 1. a) Design methodology of SMAs with 2D conjugated central units. b) Chemical structures of CH6F, CHFN, and CH17. c) Theoretically calculated frontier orbital charge density differences (ΔQ). d) Total stacking number per unit volume for the CH6F, CHFN, and CH17 systems. e) UV–vis spectra for CH6F, CHFN, and CH17 in solutions and solid films.

2. Results and Discussion

2.1. Physicochemical Properties

Three SMAs of CH6F, CHFN, and CH17 with different terminal packing areas (see chemical structures in **Figure** 1b) were studied and compared herein. The asymmetric molecular conformation of CHFN should have an effect on the frontier molecular orbitals; therefore, the density functional theory (DFT) calculation was conducted first. In general, a desirable A-D-A architecture can be indicated by the clear peak-valley-peak shape of frontier orbital charge density differences (ΔQ) for all three SMAs (Figure 1c; Figure S1, Supporting Information), which is helpful to improve light harvesting of molecules, charge generation/transport dynamics, and PCEs in resulting OSCs.[28] Due to the asymmetric geometry, the electron-donating center of CHFN is off-center compared to that of CH6F and CH17. This also causes the deflection of the dipole moment direction of CHFN (Figure S2, Supporting Information). As shown in Table S1 (Supporting Information), CH6F, CHFN, and CH17 exhibit stepwise enlarged intermolecular interactions, which may benefit from the increasing trend of dipole moments. Please note that the large dipole moment is beneficial for enhancing intermolecular packing, but it is not the only determining factor. For example, the

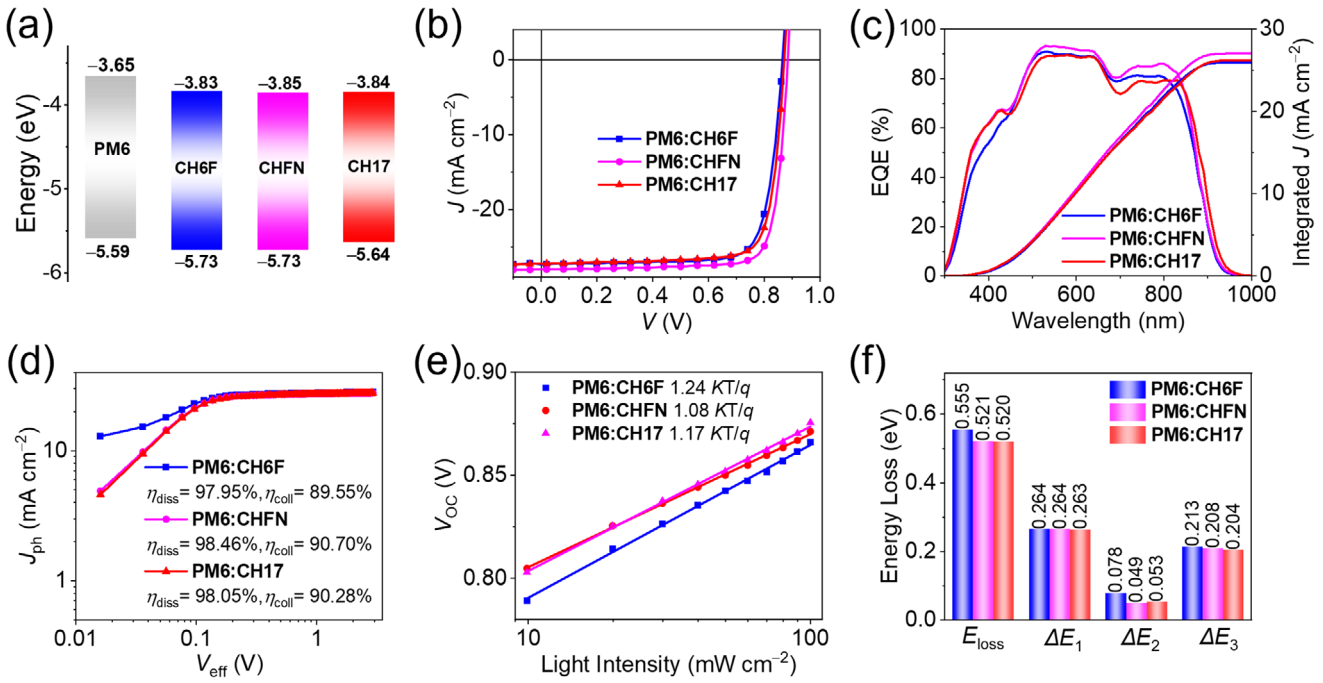

Figure 2. a) Energy levels of PM6, CH6F, CHFN, and CH17 derived from CV measurements. b) *J–V* curves for champion OSCs. c) EQE plots and integrated J_{SC} curves. d) J_{ph} versus V_{eff} curves indicating η_{diss} and η_{coll}. e) Light intensity (P_{light}) dependence of Voc. f) Statistical diagram of detailed E_{loss} of PM6:CH6F, PM6:CHFN, and PM6:CH17-based devices.

dipole moment will be significantly reduced due to the cancellation of the symmetry effect, especially for the highly symmetric organic molecules. As expected, the π–π stacking distances ($d_{\pi-\pi}$) of CH6F (3.67 Å), CHFN (3.65 Å), and CH17 (3.59 Å) decreased stepwise with the increase of effective packing areas of the end unit (Figures S4 and S5, Table S2 , Supporting Information). Moreover, the crystal coherence length (CCL) of CHFN (17.14 Å) has a slight enlargement compared to that of CH6F (16.63 Å) and CH17 (16.63 Å), indicative of the better interlayer lattice ordering in the CHFN film. The enhanced molecular packing ordering of CHFN is expected to favor efficient electron transport. This is consistent with the observed larger electron mobility (μ_e) for CHFN films (2.22×10^{-4} cm^2 V^{-1} s^{-1}) comparing to that of 1.25×10^{-4} cm^2 V^{-1} s^{-1} for CH6F and 1.82×10^{-4} cm^2 V^{-1} s^{-1} for CH17 (Figure S6, Supporting Information).

To clarify the stacking behavior of these three molecules, molecular dynamics simulations were used (Figure S7, Supporting Information). As shown in Figure S8 (Supporting Information), these three acceptor molecules were defined as three segments, labeled as A, D, and A′, resulting in the establishment of six distinct stacking modes.[29] The radial distribution functions (RDFs, g(r)) exhibit the probability of finding a particle at a certain distance from a reference particle, with higher g(r) peaks indicating a greater stacking density at specific distances. As shown in Figure S9 (Supporting Information), CH17 and CHFN exhibit significantly higher π–π stacking peaks in the AA stacking mode, indicating that the introduction of NC-2F terminals enhances molecular packing effectively. To perform a quantitative analysis, both the total number of stackings within each system and the number that were assigned to the face-on orientation were further calculated (Figure 1d; Figure S10, Supporting Information). It is clear that both the total stacking number and face-on stacking number in the AA, AD, and AA' stacking modes exhibit an enlarged trend from CH6F to CH17, indicating that the extension of terminal units promotes the intermolecular packings, which is beneficial for charge transfer.

2.2. Photovoltaic Performances

As illustrated in Figure S11 (Supporting Information), the similar but slightly decreased band gaps from CH6F (2.03 eV), CHFN (2.00 eV), to CH17 (1.98 eV) were rendered by DFT calculations, which agrees well with the stepwise red-shifted maximum absorption peaks and gradually narrowing optical band gap (Figure 1e; Table S3, Supporting Information). Moreover, the molar extinction coefficient slightly enlarges after introducing the broader NC-2F terminal, being 2.08×10^5 M^{-1} cm^{-1} for CHFN, 2.00×10^5 M^{-1} cm^{-1} for CH17, compared to 1.69×10^5 M^{-1} cm^{-1} for CH6F (Figure S12, Supporting Information). The HOMO/LUMO energy levels of CH6F, CHFN, and CH17 films were further evaluated by cyclic voltammetry (CV), being −5.73/−3.83 eV, −5.73/−3.85 eV, and −5.64/−3.84 eV, respectively (**Figure 2a**; Figure S13, Supporting Information). To avoid errors in the CV measurement, UPS measurement was employed to further characterize the HOMO energy levels and obtained similar results (Figure S14 and Table S4, Supporting Information). Given the matched energy level alignment and absorption ranges (Figure S15, Supporting Information), PM6 donor[30] was applied to fabricate OSCs with a conventional structure. The device optimization processes were enumerated in Supporting Information (Tables S5–S7, Supporting Information), and the

Table 1. Summary of photovoltaic parameters for OSCs.

Active layers[a)]	V_{OC} [V]	J_{SC} [mA cm^{-2}]	Cal. J_{SC}[b)] [mA cm^{-2}]	FF [%]	PCE [%]
PM6:CH6F	0.865	27.32	25.97	79.30	18.74
	(0.864 ± 0.004)	(27.19 ± 0.18)		(78.97 ± 0.79)	(18.55 ± 0.16)
PM6:CHFN	0.884	27.96	27.06	81.86	20.23
	(0.883 ± 0.002)	(28.09 ± 0.07)		(81.21 ± 0.22)	(20.14 ± 0.06)
PM6:CH17	0.871	27.21	26.23	80.16	19.00
	(0.872 ± 0.030)	(27.16 ± 0.22)		(79.62 ± 0.43)	(18.86 ± 0.09)

[a)] Average parameters derived from 15 independent OSCs (Tables S5–S7, Supporting Information); [b)] Current densities by integrating EQE plots.

optimal current density voltage (*J*-*V*) characteristics were shown in Figure 2b and **Table 1**. For CH6F-based binary OSCs, a PCE of 18.74% with a V_{OC} (open-circuit voltage) of 0.865 V, a J_{SC} (short-circuit current density) of 27.32 mA cm^{-2} and an fill factor (FF) of 79.30% is afforded. After replacing two IC-2F terminals with NC-2F terminals, a comparable PCE of 19.00% is achieved by CH17-based devices with J_{SC} of 27.21 mA cm^{-2}, FF of 80.16% and a slightly improved V_{OC} of 0.871 V. More excitingly, a champion PCE of 20.23% was reached by CHFN-based OSCs along with a V_{OC} of 0.884 V, J_{SC} of 27.96 mA cm^{-2} and FF of 81.86%, which is one of the highest PCEs for asymmetric acceptor-based binary OSCs (Table S8, Supporting Information). It is interesting that CHFN and CH17 present the slightly down-shifted LUMOs compared to CH6F; however, the obviously larger V_{OC}. This should be attributed to their surprisingly smaller E_{loss} of CHFN and CH17-based OSCs (discussed in detail below). Furthermore, as shown in Figure S16 (Supporting Information), PM6:CHFN-based OSCs with 1.0 cm^2 active area delivered a superior efficiency of 18.09%, with a J_{SC} of 27.82 mA cm^{-2}, a V_{OC} of 0.874 V, and an FF of 74.42%, suggesting the CHFN is a promising acceptor candidate for large-scale applications.

The external quantum efficiency (EQE) plots were recorded in Figure 2c. A gradually increasing trend can be observed from CH6F, CH17 to CHFN-based OSCs, yielding the integrated J_{SC}s of 25.97, 26.23, and 27.06 mA cm^{-2}, respectively. In order to disclose the underlying reasons for the largest EQE of CHFN-based OSCs, the exciton dissociation (P_{diss}) and charge collection (P_{coll}) efficiencies were calculated through measuring the dependence of photocurrent density (J_{ph}) versus effective voltage (V_{eff}).[31] As displayed in Figure 2d, all three systems showed excellent P_{diss}/P_{coll} in accordance with their high PCEs. However, the slightly improved values of P_{diss}/P_{coll} can be estimated as 98.46%/90.70% for CHFN compared to that of CH6F (97.95%/89.55%) and CH17 (98.05%/90.28%). Additionally, the photoluminescence (PL) quenching measurement was employed to compare the charge transfer efficiency. As shown in Figure S17 (Supporting Information), the CHFN-based system exhibits the highest PL quenching efficiency of 96.56% to those of CH6F-based and CH17-based systems, which is consistent with the high P_{diss} of CHFN. Moreover, the charge transport properties were investigated by employing the space charge limited current (SCLC) method.[32] As shown in Figure S18 (Supporting Information), electron mobility (μ_e)/hole mobility (μ_h) of PM6:CH6F, PM6:CH17, and PM6:CHFN could be determined as 3.69/3.00, 4.42/3.65, and 5.92/5.32 × 10^{-4} cm^2 V^{-1} s^{-1}, respectively, giving rise to the μ_e/μ_h ratios of 1.23, 1.21, and 1.11. The PM6:CHFN device exhibited not only the improved charge/hole mobility, but also the more balanced μ_e/μ_h ratio, which could also facilitate the charge transport in blends and improve J_{SC} and FF in resulting OSCs.[33] By measuring the dependence of V_{OC} and J_{SC} on light intensity (Figure 2e), the gradually decreased $S/(KT/q)$ from CH6F (1.24), CH17 (1.17) to CHFN (1.08) suggests the reduced trap-assisted charge recombination in CHFN-based OSCs.[34,35] The comprehensive combination of these advanced factors above determines that CHFN-based OSCs exhibit a higher EQE response.

With the aim of unveiling the reason that CHFN and CH17-based OSCs obtained the larger V_{OC} compared to CH6F under similar band gaps, a detailed energy loss analysis was carried out (Figure 2f). By applying the detailed balanced theory,[36] the total E_{loss} was partitioned into three parts, as described below:

$$\Delta E_{loss} = \Delta E_1 + \Delta E_2 + \Delta E_3 \quad (1)$$

$$\Delta E_1 = E_g - qV_{OC}^{SQ} \quad (2)$$

$$\Delta E_2 = qV_{OC}^{SQ} - qV_{OC}^{rad} \quad (3)$$

$$\Delta E_3 = qV_{OC}^{rad} - qV_{OC} \quad (4)$$

herein, the E_g is estimated by the cross-point of normalized absorption and emission spectra of neat film,[37] being ≈1.41 eV for three systems (Figure S19, Supporting Information). Therefore, the first part of energy losses (ΔE_1) for three devices, which correspond to the unavoidable radiative loss resulting from absorption above the bandgap, are also similar (≈0.264 eV). The ΔE_2s, caused by the additional radiative recombination loss below the bandgap,[38] are 0.078, 0.049, and 0.053 eV for PM6:CH6F, PM6:CHFN, and PM6:CH17, respectively. As for the most concerned nonradiative recombination energy loss of ΔE_3, it can be estimated through the following formula:[39]

$$\Delta E_3 = -ktln\left(EQE_{EL}\right) \quad (5)$$

herein, EQE_{EL} represents the electroluminescence EQEs, which are regarded as a good indicator for nonradiative energy loss.[40,41] As shown in Table S9 (Supporting Information), the obviously decreased ΔE_3 for CHFN (0.198 eV) and CH17 (0.189 eV) based devices compared to that of CH6F (0.220 eV) could be observed. The results were confirmed by their EQE_{EL} values (Figure S20, Supporting Information), in which CHFN and CH17-based devices showed obviously higher EQE_{EL} than CH6F-based devices.

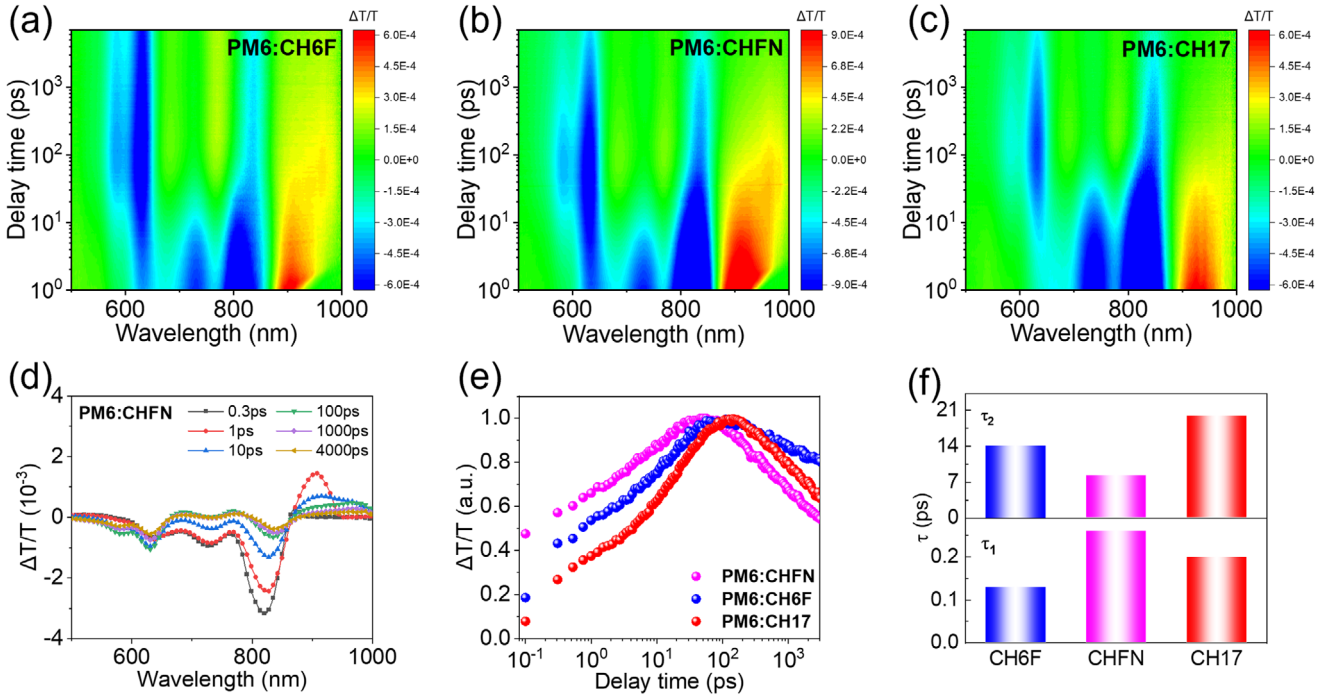

Figure 3. a–c) Contour plots of the time-resolved absorption difference spectra of the blend films. d) TA spectra of the blend films at different delay times; e) Rising kinetics observed at 630 nm, indicative of the hole transfer process. f) Statistical graphs of charge-transfer time and lifetime achieved through exponential fitting in corresponding conditions.

Moreover, the Stokes shift was also calculated to study the influence of molecular structure on energy losses. As shown in Table S10 (Supporting Information), CH6F, CHFN, and CH17 exhibit gradually decreased Stokes shifts. This implied the enhanced molecular rigidity, which could potentially contribute to the improved molecular packings.[42] It is worth noting that in these three high-performance systems, their photodynamic properties should already be quite excellent. The differences in photovoltaic parameters are usually caused by multiple factors that only show the minor advantages for the better systems, for example, PM6:CHFN-based OSCs compared to PM6:CH6F and PM6:CH17-based ones.

2.3. Charge Dynamics

The charge dynamics, including exciton transport and charge generation, were investigated by employing transient absorption spectroscopy (TA).[43] Due to the distinct absorption regions of donor and acceptor, the 800 nm pump beam was utilized to excite the acceptor exclusively in three blends. As shown in **Figure 3**a–c, the ground-state bleaching (GSB) peaks of the pristine acceptor films are located in the range of 550–870 nm. Upon photoexcitation, the TA signal of donor/acceptor blends around 830 nm appeared immediately and then rapidly decayed, accompanied by the emergence of a new bleaching peak at 630 nm, which belonged to the signal of PM6 (Figure 3d; Figure S22, Supporting Information). This indicated the process by which the hole on the excited acceptor transfers to the PM6 donor.[44] By further fitting the absorption decay at 630 nm with an exponential decay function (Figure 3e), we determined the characteristic time constants τ_1 and τ_2 that correspond to the distinct processes of hole transport dynamics. Figure 3f presented the $_1$ and τ_2 of PM6:CH6F (τ_1 = 0.13 ± 0.02 ps, τ_2 = 14.02 ± 0.46 ps), PM6:CHFN (τ_1 = 0.26 ± 0.06 ps, τ_2 = 8.31 ± 0.34 ps) and PM6:CH17 (τ_1 = 0.20 ± 0.02 ps, τ_2 = 20.01 ± 0.34 ps). Generally, the τ_1 represents the time of the rapid process linked to exciton dissociation at D/A interface, while the time of slower process for exciton diffusion to the D/A interface from bulky phases is represented as τ_2.[45] It was observed that the three systems have similar rapid processes, but the CH17-based system has an obviously larger exciton diffusion time, which may relate to the relatively inferior D/A interpreting structure in PM6:CH17 blends (discussed below).

2.4. Morphology Analysis

The charge transfer/transport behaviors in blended films and even the photovoltaic performances of OSCs are largely determined by the nanoscale morphology of active layers.[46] Thus, we employed the atomic force microscopy-based infrared spectroscopy (AFM-IR) to investigate the surficial morphology and D/A interpretation of blended films.[47] As shown in Figure S23 (Supporting Information), the smooth surface indicated by a relatively small root-mean-square roughness (R_q) of ≈0.8 nm could be observed for all three blends. A wavenumber of 2216 cm^{-1} corresponding to the stretching vibration of C≡N bond was selected to probe acceptor domains. As shown in **Figure 4**a–c, an evident D/A interpenetrating structure was observed for all the samples. Interestingly, PM6:CH6F and PM6:CHFN blends further

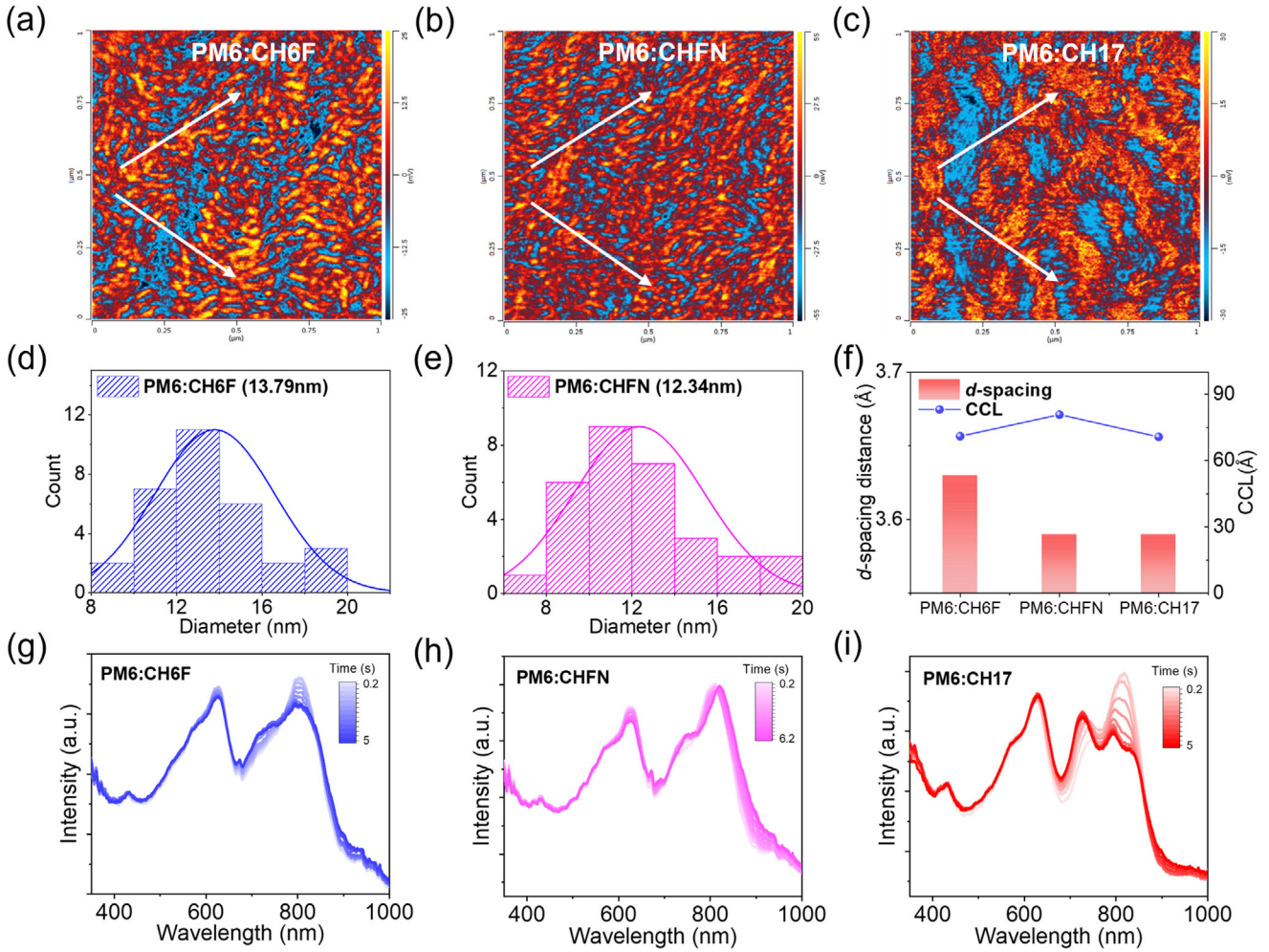

Figure 4. a–c) AFM-IR phase images of three blended films by detecting 2216 cm^{-1} signal of acceptors, in which donor and acceptor domains were marked with blue and red colors, respectively. d, e) Statistical distribution of phase separation sizes. f) Crystal coherence length (CCL) and *d*-spacing distance in π–π stacking direction (010) in blend films. g–i) Color mapping of in situ UV–vis absorption spectra with thermal annealing temperature of 90 °C.

illustrate the obvious D/A interpenetrating fibrillary networks at the nanoscale, which are proven to accelerate charge migration.[48] Only for the systems that possess obvious fibrillary structures, a statistical analysis of fiber sizes can be performed, providing the meaningful phase separation information (Figure S24, Supporting Information). Herein, PM6:CH6F and PM6:CHFN blends displayed the fiber diameters of 13.79 and 12.34 nm, respectively (Figure 4d,e). The slightly different phase separation sizes should determine the charge dynamics difference in blended films as discussed above. As for PM6:CH17 blends, a larger phase separation and inferior D/A interpenetrating structure could be rendered, which is consistent with the obviously larger exciton diffusion time compared to that of PM6:CH6F and PM6:CHFN. Obviously, the sharp contrast in PM6:CH17 film morphology is caused by the enhanced packing strength of end units for CH17.

To further study the molecular packing and orientation in films, grazing-incidence wide-angle X-ray scattering (GIWAXS) characterization on blended films was performed. Compared to the SMAs neat films (Figure S25, Table S11, Supporting Information), the sharp (010) diffraction peaks and (100) diffraction peaks can still be maintained in OOP and IP directions, respectively, after blending with PM6 donor, suggesting the desirable face-on orientation in D/A blended films. Note that the (010) diffraction peaks in the OOP direction for PM6:CHFN and PM6:CH17 blends are located at 1.75 $Å^{-1}$ with a smaller π–π packing distance of 3.59 Å compared to that of PM6:CH6F (3.63 Å) (Figure 4f), suggesting the expected enhancement of molecular π–π stacking after introducing NC-2F terminals. Unexpectedly, PM6:CHFN shows the largest CCL of 80.78 Å in the IP direction, while the smallest one of 21.75 Å in the OOP direction. Therefore, the better charge transport for PM6:CHFN may be mainly determined by the suitable D/A separation and a better fibrous D/A interpenetrating network. Then, the in situ thermal annealing absorption spectra of PM6:CH6F, PM6:CHFN, and PM6:CH17 blends were depicted in Figure 4g–i and Figure S26 (Supporting Information) to analyze the molecular crystallization dynamics.[49,50] During the thermal annealing process, the intensity and shape of

the absorption of the maximum absorption peak show only minor changes for PM6:CHFN, especially for the acceptor absorptions. This suggests the more stable pre-aggregation structure of PM6:CHFN, which agrees with the improved long-term stability of the resulting OSCs (Figure S27, Supporting Information).

3. Conclusion

With the aim of delicately tuning molecular packing behavior and photophysical properties, an asymmetric acceptor of CHFN is constructed by tuning the effective packing areas of end/central units on a 2D extended SMA platform. Compared to CH6F with two smaller IC terminals, the introduction of a larger terminal of NC-2F in CHFN and CH17 leads to the extended and more rigid conjugated backbones and redshifted absorptions. Especially for CHFN with both IC and NC-2F terminals, the more balanced packing strength of end/central units contributes to more suitable crystallinity and optimized fibrillary network morphology, which facilitates the charge transfer/transport in blended films. Consequently, PM6:CHFN-based OSCs reach a first-class efficiency of 20.23% with simultaneous improvements in V_{OC}, $J_{SC,}$ and FF, significantly outperforming their control devices (18.74% for PM6:CH6F- and 19.00% for PM6:CH17). Note that this is also one of the best values for binary OSCs based on asymmetric acceptors. In addition, PM6:CHFN achieved an excellent PCE of 18.09% for OSCs with 1.0 cm^2 active layer area, demonstrating its good potential for up-scalability. Our work deepened insight into the great significance of end/central unit packing balance and will stimulate more efforts to synergistically tune the relative packing areas of central and terminal units in high-performance SMA systems.

Supporting Information

Supporting Information is available from the Wiley Online Library or from the author.

Acknowledgements

P.W. and X.C. contributed equally to this work. The authors gratefully acknowledge the financial support from the Ministry of Science and Technology of the People's Republic of China (National Key R&D Program of China, 2023YFE0210400), National Natural Science Foundation of China (22361132530, 52025033, 52373189, 22479081, 22309090, 22204119, 22474089), Natural Science Foundation of Tianjin (23JCZDJC01160) and Haihe Laboratory of Sustainable Chemical Transformations.

Conflict of Interest

The authors declare no conflict of interest.

Data Availability Statement

The data that support the findings of this study are available from the corresponding author upon reasonable request.

Keywords

asymmetric electron acceptor, energy loss, intermolecular packing, organic photovoltaic

Received: July 14, 2025
Revised: August 26, 2025
Published online: September 20, 2025

[1] M. Deng, L. Tan, H. Tang, Q. Peng, *Chem. Commun.* **2025**, *61*, 9569.
[2] A. Polman, M. Knight, E. C. Garnett, B. Ehrler, W. C. Sinke, *Science* **2016**, *352*, aad4424.
[3] K. Jiang, Q. Wei, J. Y. L. Lai, Z. Peng, H. K. Kim, J. Yuan, L. Ye, H. Ade, Y. Zou, H. Yan, *Joule* **2019**, *3*, 3020.
[4] Y. Jiang, S. Sun, R. Xu, F. Liu, X. Miao, G. Ran, K. Liu, Y. Yi, W. Zhang, X. Zhu, *Nat. Energy* **2024**, *9*, 975.
[5] F. Sun, J. Wu, B. Cheng, L. Kan, F. Hua, W. Sun, H. Wang, Y. Huo, S. Chen, X. Xia, X. Du, F. Liu, E. Wang, X. Guo, Y. Li, M. Zhang, *Energy Environ. Sci.* **2025**, *18*, 7071.
[6] K. Liu, Y. Jiang, F. Liu, G. Ran, M. Wang, W. Wang, W. Zhang, Z. Wei, J. Hou, X. Zhu, *Adv. Mater.* **2025**, *37*, 2413376.
[7] H. Chen, Y. Huang, R. Zhang, H. Mou, J. Ding, J. Zhou, Z. Wang, H. Li, W. Chen, J. Zhu, Q. Cheng, H. Gu, X. Wu, T. Zhang, Y. Wang, H. Zhu, Z. Xie, F. Gao, Y. Li, Y. Li, *Nat. Mater.* **2025**, *24*, 444.
[8] C. Li, J. Song, H. Lai, H. Zhang, R. Zhou, J. Xu, H. Huang, L. Liu, J. Gao, Y. Li, M. H. Jee, Z. Zheng, S. Liu, J. Yan, X.-K. Chen, Z. Tang, C. Zhang, H. Y. Woo, F. He, F. Gao, H. Yan, Y. Sun, *Nat. Mater.* **2025**, *24*, 433.
[9] Y. Gong, S. Tan, X. Li, S. Qin, X. Li, T. Zou, Y. Li, M. Yuan, Z. Zhang, H. Hu, T. Liang, J. Zhang, L. Meng, F. Liu, Y. Li, *Angew. Chem., Int. Ed.* **2025**, *64*, 202505366.
[10] L. Wu, T. Pan, X. Wang, Y. Hai, S. Liu, R. Ma, J. Lu, L. Xiong, Y. Chan, J. Dong, Y. Li, Y. Luo, L. Zhu, B. Xiao, J. Zhang, J. Chen, T. Zhang, J. Wu, S. Liu, T. Jia, F. Huang, *Angew. Chem., Int. Ed.* **2025**, *64*, 202506445.
[11] C. Li, J. Zhou, J. Song, J. Xu, H. Zhang, X. Zhang, J. Guo, L. Zhu, D. Wei, G. Han, J. Min, Y. Zhang, Z. Xie, Y. Yi, H. Yan, F. Gao, F. Liu, Y. Sun, *Nat. Energy* **2021**, *6*, 605.
[12] L. Zhu, M. Zhang, G. Zhou, T. Hao, J. Xu, J. Wang, C. Qiu, N. Prine, J. Ali, W. Feng, X. Gu, Z. Ma, Z. Tang, H. Zhu, L. Ying, Y. Zhang, F. Liu, *Adv. Energy Mater.* **2020**, *10*, 1904234.
[13] W. Zhu, A. P. Spencer, S. Mukherjee, J. M. Alzola, V. K. Sangwan, S. H. Amsterdam, S. M. Swick, L. O. Jones, M. C. Heiber, A. A. Herzing, G. Li, C. L. Stern, D. M. DeLongchamp, K. L. Kohlstedt, M. C. Hersam, G. C. Schatz, M. R. Wasielewski, L. X. Chen, A. Facchetti, T. J. Marks, *J. Am. Chem. Soc.* **2020**, *142*, 14532.
[14] Y. Bai, L. Hong, Y. Dou, S. Zhu, H. Tang, D. Liu, Y. Cao, J. Chen, S. Chen, L. Shao, Z. Hu, D. Tang, K. Zhang, S.-J. Su, C. Liu, F. Huang, *ACS Energy Lett.* **2024**, *9*, 1786.
[15] Y. Zhang, M. Wang, S. Li, J. Yu, X.-K. Ye, A. Wupur, Y. Luo, J. Wu, C.-Z. Li, M. Shi, H. Chen, *CCS Chem.* **2025**, *7*, 1.
[16] R. Xu, Y. Jiang, F. Liu, G. Ran, K. Liu, W. Zhang, X. Zhu, *Adv. Mater.* **2024**, *36*, 2312101.
[17] H. Chen, Y. Zou, H. Liang, T. He, X. Xu, Y. Zhang, Z. Ma, J. Wang, M. Zhang, Q. Li, C. Li, G. Long, X. Wan, Z. Yao, Y. Chen, *Sci. China Chem.* **2022**, *65*, 1362.
[18] Y. Shi, Y. Chang, K. Lu, Z. Chen, J. Zhang, Y. Yan, D. Qiu, Y. Liu, M. A. Adil, W. Ma, X. Hao, L. Zhu, Z. Wei, *Nat. Commun.* **2022**, *13*, 3256.
[19] Z. Chen, J. Zhu, D. Yang, W. Song, J. Shi, J. Ge, Y. Guo, X. Tong, F. Chen, Z. Ge, *Energy Environ. Sci.* **2023**, *16*, 3119.
[20] T. Xu, G. Ran, Z. Luo, Z. Chen, J. Lv, G. Zhang, H. Hu, W. Zhang, C. Yang, *Small* **2024**, *20*, 2405476.
[21] K. Liu, Y. Jiang, G. Ran, F. Liu, W. Zhang, X. Zhu, *Joule* **2024**, *8*, 835.
[22] Z. Luo, W. Wei, R. Ma, G. Ran, M. H. Jee, Z. Chen, Y. Li, W. Zhang, H. Y. Woo, C. Yang, *Adv. Mater.* **2024**, *36*, 2407517.
[23] X. Bi, X. Cao, T. He, H. Liang, Z. Yao, J. Yang, Y. Guo, G. Long, B. Kan, C. Li, X. Wan, Y. Chen, *Small* **2024**, *20*, 2401054.

[24] Y. Zou, H. Chen, X. Bi, X. Xu, H. Wang, M. Lin, Z. Ma, M. Zhang, C. Li, X. Wan, G. Long, Y. Zhaoyang, Y. Chen, *Energy Environ. Sci.* **2022**, *15*, 3519.
[25] C. He, Z. Chen, T. Wang, Z. Shen, Y. Li, J. Zhou, J. Yu, H. Fang, Y. Li, S. Li, X. Lu, W. Ma, F. Gao, Z. Xie, V. Coropceanu, H. Zhu, J.-L. Bredas, L. Zuo, H. Chen, *Nat. Commun.* **2022**, *13*, 2598.
[26] X. Cao, P. Wang, X. Jia, W. Zhao, H. Chen, Z. Xiao, J. Li, X. Bi, Z. Yao, Y. Guo, G. Long, C. Li, X. Wan, Y. Chen, *Angew. Chem., Int. Ed.* **2025**, *64*, 202417244.
[27] M. Deng, X. Xu, Y. Duan, W. Qiu, L. Yu, R. Li, Q. Peng, *Adv. Mater.* **2024**, *36*, 2308216.
[28] X. Wan, C. Li, M. Zhang, Y. Chen, *Chem. Soc. Rev.* **2020**, *49*, 2828.
[29] W. Zhao, A. Li, Y. Zhou, Z. Hao, J. Yang, T. Yan, X. Wan, X. Chen, Y. Chen, G. Long, *ACS Appl. Mater. Interfaces* **2025**, *17*, 45947.
[30] M. Zhang, X. Guo, W. Ma, H. Ade, J. Hou, *Adv. Mater.* **2015**, *27*, 4655.
[31] Y. Jiang, Y. Li, F. Liu, W. Wang, W. Su, W. Liu, S. Liu, W. Zhang, J. Hou, S. Xu, Y. Yi, X. Zhu, *Nat. Commun.* **2023**, *14*, 5079.
[32] M. Deng, X. Xu, Y. Duan, L. Yu, R. Li, Q. Peng, *Adv. Mater.* **2023**, *35*, 2210760.
[33] D. Qiu, H. Zhang, C. Tian, J. Zhang, L. Zhu, Z. Wei, K. Lu, *Adv. Mater.* **2023**, *35*, 2307398.
[34] L. J. A. Koster, V. D. Mihailetchi, R. Ramaker, P. W. M. Blom, *Appl. Phys. Lett.* **2005**, *86*, 123509.
[35] S. Zeiske, O. J. Sandberg, N. Zarrabi, W. Li, P. Meredith, A. Armin, *Nat. Commun.* **2021**, *12*, 3603.
[36] J. Yao, T. Kirchartz, M. S. Vezie, M. A. Faist, W. Gong, Z. He, H. Wu, J. Troughton, T. Watson, D. Bryant, J. Nelson, *Phys. Rev. Appl.* **2015**, *4*, 014020.
[37] D. Yang, Y. Wang, T. Sano, F. Gao, H. Sasabe, J. Kido, *J. Mater. Chem. A* **2018**, *6*, 13918.
[38] L. Zhan, S. Li, Y. Li, R. Sun, J. Min, Z. Bi, W. Ma, Z. Chen, G. Zhou, H. Zhu, M. Shi, L. Zuo, H. Chen, *Joule* **2022**, *6*, 662.
[39] S. Liu, J. Yuan, W. Deng, M. Luo, Y. Xie, Q. Liang, Y. Zou, Z. He, H. Wu, Y. Cao, *Nat. Photonics* **2020**, *14*, 300.
[40] X.-K. Chen, D. Qian, Y. Wang, T. Kirchartz, W. Tress, H. Yao, J. Yuan, M. Hülsbeck, M. Zhang, Y. Zou, Y. Sun, Y. Li, J. Hou, O. Inganäs, V. Coropceanu, J.-L. Bredas, F. Gao, *Nat. Energy* **2021**, *6*, 799.
[41] R. Englman, J. Jortner, *Mol. Phys.* **1970**, *18*, 145.
[42] X. Gu, Y. Wei, R. Zeng, J. Lv, Y. Hou, N. Yu, S. Tan, Z. Wang, C. Li, Z. Tang, Q. Peng, F. Liu, Y. Cai, X. Zhang, H. Huang, *Angew. Chem., Int. Ed.* **2025**, *64*, 202418926.
[43] M. Zhang, Z. Wang, L. Zhu, R. Zeng, X. Xue, S. Liu, J. Yan, Z. Yang, W. Zhong, G. Zhou, L. Kan, J. Xu, A. Zhang, J. Deng, Z. Zhou, J. Song, H. Jing, S. Xu, Y. Zhang, F. Liu, *Adv. Mater.* **2024**, *36*, 2407297.
[44] X. Ran, C. Zhang, D. Qiu, A. Tang, J. Li, T. Wang, J. Zhang, Z. Wei, K. Lu, *Adv. Mater.* **2025**, *37*, 2504805.
[45] F. Liu, Y. Jiang, R. Xu, W. Su, S. Wang, Y. Zhang, K. Liu, S. Xu, W. Zhang, Y. Yi, W. Ma, X. Zhu, *Angew. Chem., Int. Ed.* **2024**, *63*, 202313791.
[46] F. Zhao, C. Wang, X. Zhan, *Adv. Energy Mater.* **2018**, *8*, 1703147.
[47] R. Zeng, M. Zhang, X. Wang, L. Zhu, B. Hao, W. Zhong, G. Zhou, J. Deng, S. Tan, J. Zhuang, F. Han, A. Zhang, Z. Zhou, X. Xue, S. Xu, J. Xu, Y. Liu, H. Lu, X. Wu, C. Wang, Z. Fink, T. P. Russell, H. Jing, Y. Zhang, Z. Bo, F. Liu, *Nat. Energy* **2024**, *9*, 1117.
[48] L. Zhu, M. Zhang, J. Xu, C. Li, J. Yan, G. Zhou, W. Zhong, T. Hao, J. Song, X. Xue, Z. Zhou, R. Zeng, H. Zhu, C.-C. Chen, R. C. I. MacKenzie, Y. Zou, J. Nelson, Y. Zhang, Y. Sun, F. Liu, *Nat. Mater.* **2022**, *21*, 656.
[49] J. Song, Y. Li, Y. Cai, R. Zhang, S. Wang, J. Xin, L. Han, D. Wei, W. Ma, F. Gao, Y. Sun, *Matter* **2022**, *5*, 4047.
[50] H. Chen, W. Sun, R. Zhang, Y. Huang, B. Zhang, G. Zeng, J. Ding, W. Chen, F. Gao, Y. Li, Y. Li, *Adv. Mater.* **2024**, *36*, 2402350.